ISSN 0031-918X, Physics of Metals and Metallography, 2017, Vol. 118, No. 5, pp. 494–506. © Pleiades Publishing, Ltd., 2017.
Original Russian Text © V.V. Sagaradze, T.N. Kochetkova, N.V. Kataeva, K.A. Kozlov, V.A. Zavalishin, N.F. Vil'danova, V.S. Ageev, M.V. Leont'eva-Smirnova, A.A. Nikitina, 2017, published in Fizika Metallov i Metallovedenie, 2017, Vol. 118, No. 5, pp. 522–534.

STRENGTH AND PLASTICITY

Structure and Creep of Russian Reactor Steels with a BCC Structure

V. V. Sagaradze[a], *, T. N. Kochetkova[a], N. V. Kataeva[a], K. A. Kozlov[a], V. A. Zavalishin[a], N. F. Vil'danova[a], V. S. Ageev[b], M. V. Leont'eva-Smirnova[b], and A. A. Nikitina[b]

[a] *Mikheev Institute of Metal Physics, Ural Branch, Russian Academy of Sciences, ul. S. Kovalevskoi 18, Ekaterinburg, 620990 Russia*

[b] *Bochvar High-Technology Scientific Research Institute for Inorganic Materials, ul. Rogova 5a, Moscow, 123060 Russia*

**e-mail: vsagaradze@imp.uran.ru*

Received July 12, 2016; in final form, October 10, 2016

Abstract—The structural phase transformations have been revealed and the characteristics of the creep and long-term strength at 650, 670, and 700°C and 60–140 MPa have been determined in six Russian reactor steels with a bcc structure after quenching and high-temperature tempering. Creep tests were carried out using specially designed longitudinal and transverse microsamples, which were fabricated from the shells of the fuel elements used in the BN-600 fast neutron reactor. It has been found that the creep rate of the reactor bcc steels is determined by the stability of the lath martensitic and ferritic structures in relation to the diffusion processes of recovery and recrystallization. The highest-temperature oxide-free steel contains the maximum amount of the refractory elements and carbides. The steel strengthened by the thermally stable Y–Ti nanooxides has a record high-temperature strength. The creep rate at 700°C and 100 MPa in the samples of this steel is lower by an order of magnitude and the time to fracture is 100 times greater than that in the oxide-free reactor steels.

Keywords: reactor steels, bcc lattice, structure, carbides, Y–Ti nanooxides, creep rate, long-term strength, electron microscopy, mechanical properties

DOI: 10.1134/S0031918X17050131

INTRODUCTION

Nowadays, the shells of fuel elements (FEs) of fast neutron reactors of the BN-600 type are fabricated from austenite ChS-68 steel (16Cr–15Ni–3Mo–Mn–Ti–V–B) [1, 2]. Other reactor steels with an fcc structure are developed [3–7]. These steels are plastic and have a fairly high long-term strength at 500–700°C, but are prone to the vacancy swelling at high doses of the neutron irradiation. Therefore, there is a tendency to replace them with ferritic and ferritic–martensitic stainless steels with a bcc structure [8–12]. These steels have a higher resistance to vacancy swelling and usually exhibit a lower activity after neutron irradiation due to the absence of long-lived isotopes. In the ferritic–martensitic steels with 12–17% chromium upon irradiation by fast neutrons, as a result of the formation of a large amount of point defects, an accelerated separation of the α solid solution is observed with the isomorphic precipitation of the dispersed high-chromium α' phase with a bcc structure with lattice parameters close to those of the α matrix. The elastic stresses that arise around the α' phase, just as around the γ' phase in the titanium-containing austenitic steels of the Kh16N15MT1 type, contribute to the recombination of point defects, which decreases the pore formation [13–15]. At the same time, the dissolution of the α' particles in the displacement cascades occurs. Apparently, in this case, the process of the radiation-induced precipitation–dissolution of α' particles is not completed for a long time, which significantly delays the onset of intense pore formation. The low-activated reactor stainless steels with a bcc structure can be used as the structural material for blanket and working chamber of fusion reactors. However, the above-mentioned steels have lower high-temperature strength and are more prone to the loss of plasticity and to an embrittlement under neutron irradiation as compared to the austenitic reactor steels. In the present paper, we assume to carry out a comparative study of the thermal creep, long-term strength, and structural phase transformations at 650–700°C in the Russian reactor steels with a bcc structure. It should be noted that the highest-temperature reactor steels are oxide-dispersion strengthened (ODS) stainless steels of new generation [16–22]. The oxides of yttrium introduced into the steel matrix (using mechanical alloying and powder metallurgy) with sizes of 2–4 nm do not dissolve, even at premelting temperatures and thereby contribute to the retaining

Table 1. Chemical composition of the investigated steels, wt % (for Ta and Ce, calculated values are given)

Steel	C	Cr	Mn	Mo	Nb	V	W	Ni	N	Si	P	S	Ta	Ce	Ti	B/O	Zr/Y
EK-181	0.15	11.2	0.74	0.01	0.01	0.25	1.13	0.03	0.04	0.33	0.010	0.006	0.08	0.15	–	0.006/–	0.05/–
ChS-139	0.21	12.2	0.60	0.53	0.31	0.31	1.27	0.71	0.08	0.15	0.006	0.004	0.07	0.10	0.01	0.002/–	0.01/–
EP-450	0.13	13.0	–	2.0	0.2	0.2	–	–	–	–	–	–	–	–	–	0.006/–	–
EP-823	0.16	11.0	0.7	0.8	0.3	0.3	0.3	0.7	–	1.2	–	–	–	–	–	–	–
EP-900	0.15	11.5	0.7	0.7	0.3	0.3	0.8	0.7	–	1.1	–	–	–	0.03	–	–	–
EP-450-DUO	0.13	13.1	0.44	1.61	0.35	0.18	–	0.12	–	0.23	–	–	–	–	0.2	–/0.32	–/0.26

of high characteristics of the high-temperature strength. Therefore, the present paper is also aimed at an analysis of the structure and high-temperature strength of the oxide-containing EP-450-DUO steel [16] compared to the reactor steels that contain the carbide phase.

EXPERIMENTAL

The studies of the structure, creep, and long-term strength were performed using samples of the Russian reactor steels with a bcc structure, which were cut from the shells of the fuel elements representing tubes with an outside diameter of 6.9 mm and a wall thickness of 0.4 mm. The investigated tubes were fabricated from the martensitic steels EK-181, ChS-139 and ferritic–martensitic steels EP-450, EP-823, and EP-900. In most cases, the steels were quenched from 1100°C and tempered predominantly at 720°C for 2 h. The EP-450-DUO steel after quenching from 1150°C for 1 h and tempering at 740°C for 2 h was also studied. The chemical composition of the steels is presented in Table 1.

The process of producing EP-450-DUO steel consisted of [16] the mechanical alloying of powders in ball mills followed by compaction and sintering. The mechanical alloying of powder of EP-450 steel (13Cr–2Mo–V–Nb–B) in a mixture with particles of Y_2O_3 oxides with a size of up to 80 nm (in an amount of 0.25 wt %), which are dissolved under deformation, was carried out for 30 h in a high-energy mill in an argon atmosphere. After the milling and degassing of mechanically alloyed powder in a vacuum at 450°C, the sintering of the powder was performed during hydroextrusion at 1000–1150°C with the simultaneous precipitation of strengthening yttrium–titanium oxides with sizes of 3–5 nm.

The structure of steels was studied by transmission electron microscopy using a JEM-200CX microscope at an accelerated voltage of 160 kV. The samples were prepared by electric polishing in a solution of chromic anhydride and phosphoric acid. The phase identification was carried out using the dark-field method and selected-area electron diffraction. Using electron-microscopic images, we carried out the quantitative analysis of carbide and oxide particles. For this purpose, there was used a Siams Photolab software, by which the images were converted into a binary form and for each image the histograms of the particles-size distribution were constructed, and then an average size and number density of particles were determined.

The mechanical properties of steels were determined in short- and long-term tests at different temperatures. The production of the longitudinal and transverse microsamples from the shells of the FEs for creep tests included the cutting of pipes into samples with a length of 22 mm and subsequent longitudinal cutting of these samples by the electric spark method along the axis. Then, we straightened the samples using a lathe (with a special tool) into plates with dimensions of 22 × 22 mm (the thickness of plates remained the same as the wall thickness of the initial tube (0.4 mm)). During the straightening of the samples, the maximum surface deformation was only 6%, which hardly affected the properties of microsamples of the steel, especially in the martensitic state. For creep tests, dumbbell samples with a gage part of 7 × 2 × 0.4 mm were prepared from the plates by grinding. The plates, combined in stacks of 3–4 pieces, were processed using a grinding machine with water cooling, which provided a constant width of the gage part of the microsamples along the entire length with an accuracy of 0.01 mm. After grinding, plates of the Kh18N10 steel were spot-welded to the heads of samples. Then, holes with diameters of 6 mm for pins were drilled in the fixed heads of the samples so that they were located along the axis of the sample with a deviation that did not exceed 0.02 mm. The dumbbell samples were cut along and across the axis of the initial tube of the FEs for analyzing the anisotropy of properties upon creep tests. The creep tests were performed under direct loading using AIMA-5-2-type standard machines in the range of temperatures of 650–700°C, at a constant load. The load was determined by a weighing of the load with an error of no more than 0.1%. The temperature in a furnace during tests was maintained with an accuracy of ±3°C. The elongation of the sample during tests was recorded by two indicators of 1 MIG type with an accuracy of up to 0.001 mm.

Table 2. Mechanical properties of steels after quenching and high-temperature tempering at 720°C

Steel, initial material	Cutting direction of samples	T_{test}, °C	σ_u, MPa	$\sigma_{0.2}$, MPa	δ, %
EP-450-DUO, plates	Along	20	991	815	11.2
		650	628	567	14.9
		700	602	499	15.6
	Across	20	1057	746	8.2
		650	604	555	8.3
		700	554	526	12.6
EP-450, tubes	Along	20	867	753	14.0
		650	430	403	15.9
		700	411	367	17.2
	Across	20	860	791	12.0
		700	378	338	11.4
ChS-139, tubes	Along	20	950	843	10.0
		650	501	464	24.3
		700	411	343	24.6
	Across	20	956	861	9.0
		650	461	446	20.0
		700	421	334	24.7
EK-181, tubes	Along	20	872	806	9.6
		650	485	428	16.0
		700	368	346	22.2
	Across	20	871	778	11.1
		650	477	440	16.4
		700	379	311	29.6

RESULTS AND DISCUSSION

Mechanical Properties of Steels upon Short-Term Tests

Table 2 shows the mechanical properties of the longitudinal and transverse samples of the EK-181, ChS-139, EP-450, and EP-450-DUO steels at 20, 650, and 700°C, which were obtained in short-term tensile tests. As a rule, for longitudinal and transverse samples, close values of plasticity and ultimate tensile strength σ_u are observed at 20°C, which may indicate the absence of a pronounced anisotropy of properties in the samples subjected to high-temperature tempering. The highest values of the yield stress at 20°C were found in ChS-139 steel ($\sigma_{0.2}$ = 843–861 MPa), which can be explained by the predominant martensitic structure and the largest amounts of the interstitial elements (the carbon content in this steel was 0.21 wt %). The other oxide-free steels had somewhat smaller values of the yield stress ($\sigma_{0.2}$ = 753–806 MPa).

Figures 1a–1e show the structure of the ChS-139, EK-181, EP-450, EP-823, and EP-900 steels after quenching from 1100°C and high-temperature tempering at 720°C for 2 h. Almost all of these steels have predominantly lath structures of tempered (polygonized) martensite; in the EP-450 steel only, ferrite occupies the larger part of the bulk. In all steels, rather coarse lamellar carbides of the $M_{23}C_6$ type with predominant lengths of 50–200 nm are located at the boundaries of the martensitic laths and ferritic grains; dark-field images are presented in Figs. 1a, 1c, and 2a. Inside of martensitic and ferritic crystals, there are disperse particles of special carbides of the (V, Nb)C type with sizes of up to 10 nm, which, in particular, are observed in the dark-field image of the structure of EK-181 steel (Fig. 2b).

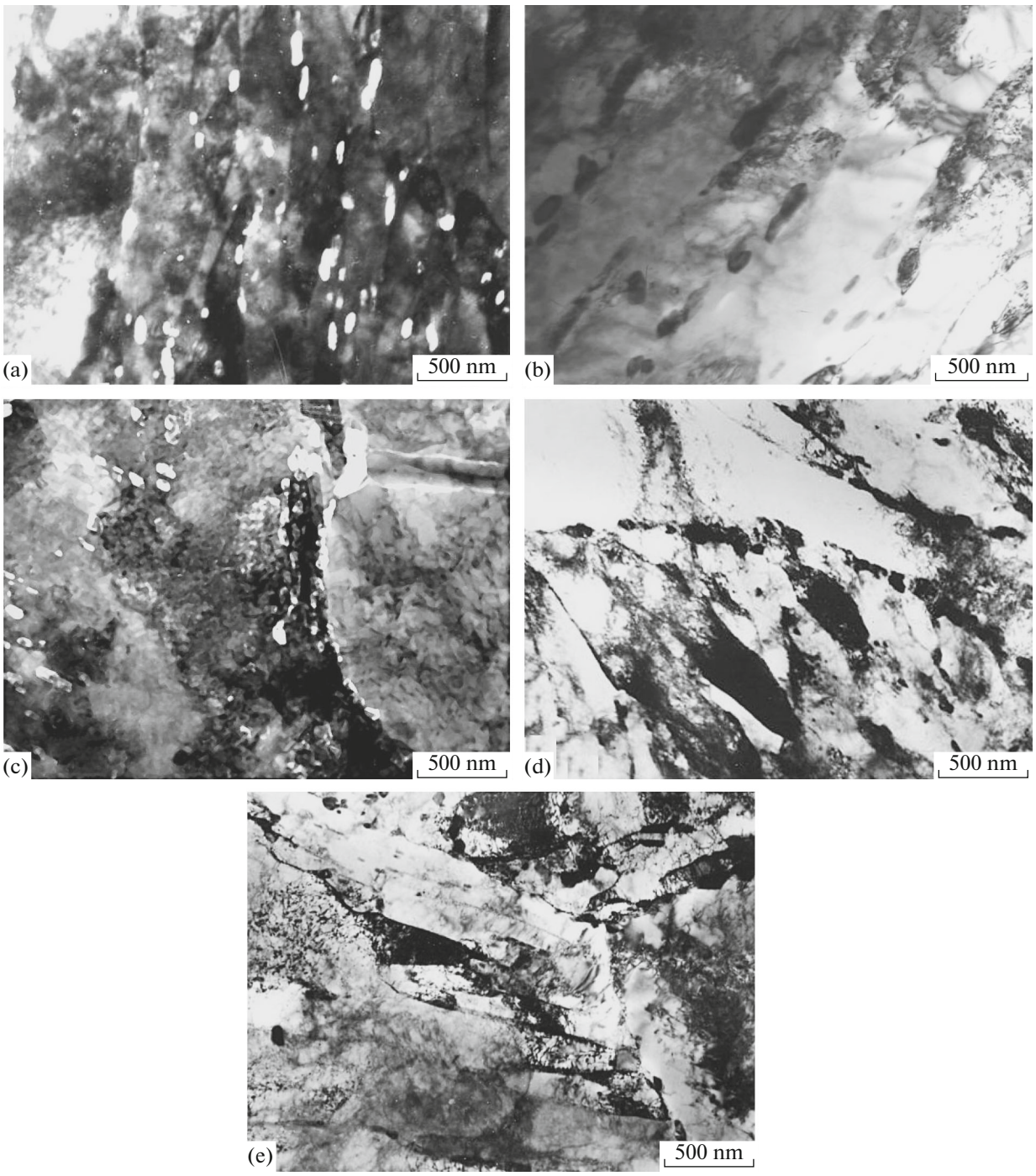

Fig. 1. Structure of tubes of steels investigated in the initial state after quenching and high-temperature tempering at 720°C for 2 h: (a) ChS-139; (b) EK-181; (c) EP-450; (d) EP-823; and (e) EP-900; (a, c) dark-field images in the reflections of the $M_{23}C_6$ phase.

The oxide-dispersion strengthened EP-450-DUO steel is slightly different in the strength characteristics from the ChS-139 steel: the values of the yield stress are close, the ultimate tensile strength is somewhat higher (σ_u = 991–1057 MPa). This is associated with the fact that it is ferrite strengthened by dispersed oxides rather than martensite is the main structural constituent [16]. However, at the higher temperature of 700°C, the yield stress of the EP-450-DUO steel is 150–200 MPa higher, even after short-term tests. Therefore, we can expect a higher high-temperature strength in the EP-450-DUO steel than in the other oxide-free steels.

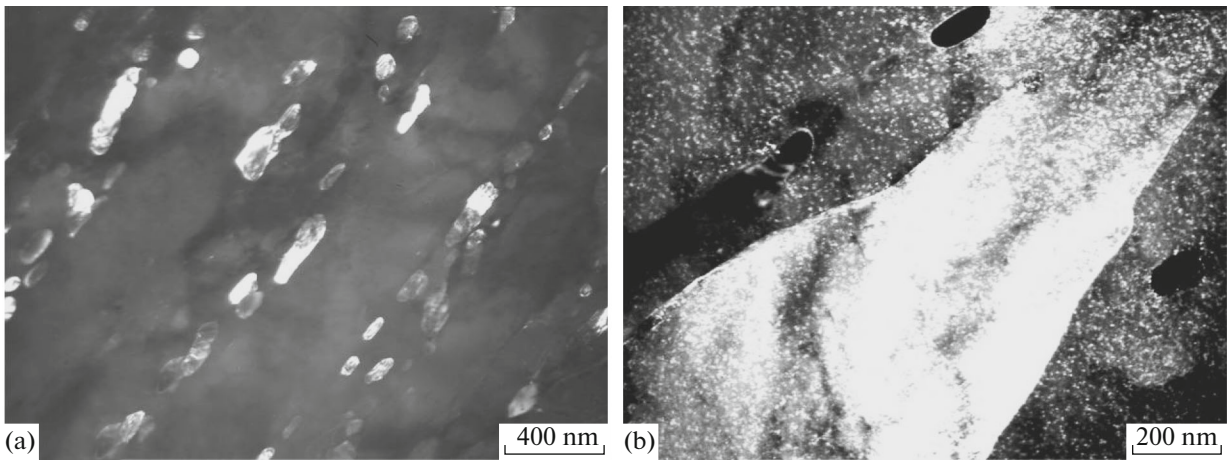

Fig. 2. Dark-field images of the carbides taken in the reflections of (a) $(440)_{Me_{23}C_6}$ and (b) $(020)_{VC}$ in EK-181 steel after quenching and high-temperature tempering at 720°C for 2 h.

Creep Resistance of the Investigated Steels

Table 3 shows the comparative data on the creep of the longitudinal and transverse samples of the EK-181 and ChS-139 steels, which were cut from shells of fuel elements of the BN-600 reactor (creep rate $\dot{\varepsilon}_2$, time to fracture τ_f, and maximum elongation $\varepsilon_{max.el}$ at 650–700°C and stresses of 100 and 140 MPa). The tests of the samples were carried out after quenching from 1100°C and high-temperature tempering at 720°C for 2 h. As can be seen in Table 3, following creep test of the reactor steels, no strong anisotropy of properties were revealed. At the low temperature (650°C) and large times of tests (thousands of hours), the transverse samples have some advantage (according to the time to fracture and creep rate). At 700°C and short

Table 3. Comparative data on the creep of the longitudinal and transverse samples of the EK-181 and ChS-139 steels, which were cut from the shells of fuel elements after quenching and high-temperature tempering

Steel	Tensile direction	T_{test}, °C	σ, MPa	$\varepsilon_{max.el}$, %	$\dot{\varepsilon}_2$, %/h	$\log\dot{\varepsilon}_2$	τ_f, h	$\log\tau_f$
EK-181	Across	700	140	15.7	1.4×10^{-1}	−0.85	31.4	1.49
		700	100	14.2	1.15×10^{-1}	−0.93	44.0	1.64
		650	140	12.8	1.41×10^{-2}	−1.85	404.0	2.64
		650	100	8.6	9.48×10^{-4}	−3.02	4061.3	3.60
	Along	700	140	17.8	3.1×10^{-1}	−0.50	18.7	1.27
		700	100	25.7	1.06×10^{-1}	−0.97	60.8	1.78
		650	140	23.0	2.27×10^{-2}	−1.64	341.0	2.53
		650	100	18.5	3.92×10^{-3}	−2.40	1990.4	3.30
Chs-139	Across	700	140	15.7	1.87×10^{-1}	−0.72	28.3	1.45
		700	100	14.2	5.47×10^{-2}	−1.26	179.3	2.25
		650	140	17.1	4.13×10^{-3}	−2.38	2541.9	3.40
		650	100	12.8	8.99×10^{-4}	−3.04	7084.0	3.85
	Along	700	140	15.7	1.39×10^{-1}	−0.85	53.4	1.72
		700	100	14.2	1.7×10^{-2}	−1.76	403.7	2.60
		650	140	14.2	3.23×10^{-3}	−2.49	2526.0	3.40
		650	100	17.1	1.90×10^{-3}	−2.70	6324.0	3.80

Table 4. Creep characteristics of the steels at 650 and 670°C (transverse samples) after quenching and high-temperature tempering

Steel	T_{test}, °C	σ, MPa	log σ	$\varepsilon_{max.el}$, %	$\dot{\varepsilon}_2$, %/h	log $\dot{\varepsilon}_2$	τ_f, h	log τ_f
EP-823	670	100	2.00	18.6	8.80×10^{-2}	−1.05	74.3	1.87
	670	80	1.90	15.7	1.75×10^{-2}	−1.75	469.8	2.67
	670	60	1.77	12.1	6.95×10^{-3}	−2.15	892.4	2.95
	650	100	2.00	14.2	1.41×10^{-2}	−1.85	258.3	2.41
	650	80	1.90	10.0	1.39×10^{-3}	−2.85	3087.3	3.48
	650	60	1.77	14.2	9.42×10^{-4}	−3.02	6286.6	3.79
EP-900	670	100	2.00	11.4	1.99×10^{-2}	−1.70	204.8	2.31
	670	80	1.90	14.2	4.34×10^{-3}	−2.36	1027.0	3.01
	670	60	1.77	11.1	7.14×10^{-4}	−3.14	5581.5	3.74
	650	100	2.00	10.0	3.26×10^{-3}	−2.48	1234.7	3.09
	650	80	1.90	10.2	1.18×10^{-3}	−2.92	2909.8	3.46
EK-181	670	120	2.07	16.2	2.26×10^{-2}	−1.64	333.8	2.52
	670	100	2.00	17.1	4.91×10^{-3}	−2.30	1135.4	3.05
	670	80	1.90	15.7	2.39×10^{-3}	−2.62	1532.5	3.18
	670	60	1.77	14.8	2.44×10^{-3}	−2.61	2519.9	3.40
	650	140	2.14	12.8	1.41×10^{-2}	−1.85	404.5	2.64
	650	100	2.00	8.6	9.48×10^{-4}	−3.02	4061.3	3.60
ChS-139	670	120	2.07	8.5	8.40×10^{-3}	−2.07	430.9	2.63
	670	100	2.000	14.3	4.80×10^{-3}	−2.31	1736.4	3.23
	670	80	1.90	19.3	1.10×10^{-3}	−2.95	5615.5	3.74
	670	60	1.77	14.3	7.50×10^{-4}	−3.12	8448.5	3.92
	650	140	2.14	17.1	4.13×10^{-3}	−2.38	2541.9	3.40
	650	100	2.00	12.8	8.99×10^{-4}	−3.04	7084.0	3.85
EP-450	650	140	2.14	12.8	2.07×10^{-3}	−2.68	1596.1	3.20
	650	100	2.00	15.6	2.00×10^{-3}	−2.69	1938.2	3.28
EP-450-ODS, plate	650	140	2.146	–	9.83×10^{-4}	−3.00	>28852.6	4.46
	650	100	2.00	–	3.04×10^{-4}	−3.51	>28428.4	4.45

tests times (tens and hundreds of hours), the longitudinal samples usually show higher properties. It should be noted that the results of the long-term tensile tests for transverse samples better describe the real behavior of steels in the reactor than the results of tests of the longitudinal samples due to the existing transverse deformation of the shells of the FEs by the gases that arise during processing.

Tables 4 and 5 present the creep characteristics (creep rate $\dot{\varepsilon}_2$, time to fracture τ_f, and maximum elongation $\varepsilon_{max.el}$) for transverse samples of all investigated steels at 650, 670, and 700°C and stresses of 60–140 MPa. Figures 3 and 4 show the dependences of the time to fracture and creep rate at 670 and 700°C on the stresses for all main investigated reactor steels with the bcc structure, which were obtained using trans-

Table 5. Creep characteristics of the steels at 700°C (transverse samples) after quenching and high-temperature tempering

Steel	T_{test}, °C	σ, MPa	log σ	$\varepsilon_{max.el}$, %	$\dot{\varepsilon}_2$, %/h	log $\dot{\varepsilon}_2$	τ_f, h	log τ_f
EP-823	700	100	2.00	21.4	8.90×10^{-1}	−0.05	8.6	0.93
	700	80	1.90	24.2	2.37×10^{-1}	−0.62	28.9	1.46
EP-900	700	100	2.00	23.0	9.1×10^{-1}	−0.04	6.6	0.81
	700	80	1.90	30.0	2.12×10^{-1}	−0.67	35.0	1.54
EK-181	700	140	2.14	15.7	1.40×10^{-1}	−0.85	31.4	1.49
	700	100	2.00	14.2	1.15×10^{-1}	−0.93	44.0	1.64
	700	80	1.90	22.8	3.57×10^{-2}	−1.44	178.1	2.25
	700	60	1.77	11.4	6.72×10^{-3}	−2.17	837.5	2.92
	700	40	1.60	25.7	3.52×10^{-3}	−2.45	2548.9	3.40
ChS-139	700	140	2.14	15.7	1.87×10^{-1}	−0.72	28.3	1.45
	700	100	2.00	14.2	5.47×10^{-2}	−1.26	179.3	2.25
	700	80	1.90	11.4	6.42×10^{-3}	−2.19	949.3	2.97
	700	60	1.77	14.2	1.18×10^{-3}	−2.92	5448.3	3.73
	700	40	1.60	13.4	1.30×10^{-3}	−2.88	6578.2	3.81
EP-450	700	140	2.14	10.0	2.00×10^{-1}	−0.69	18.2	1.26
	700	100	2.00	15.7	3.00×10^{-2}	−1.52	203.3	2.30
	700	80	1.90	13.0	6.40×10^{-3}	−2.19	790.3	2.89
EP-450-ODS, plate	700	140	2.14	11.4	6.77×10^{-2}	−1.16	132.9	2.12
	700	100	2.00	–	9.40×10^{-4}	−3.02	>27413.6	4.43

verse samples (current results of the continuing tests are indicated by arrows in the figures and by signs ">" in the tables). As the time to fracture increases at 670 and 700°C, especially at high stresses (Figs. 3a, 3b), the steels are positioned in the following order: EP-823 and EP-900; EK-181; EP-450 and ChS-139; EP-450-DUO. The EP-450 steel (*5*) according to the time to fracture at 700°C is comparable to the ChS-139 steel (*4*) (Fig. 3b). At 650°C and 10 MPa, the EP-450 steel behaves as the ChS-139 steel at the higher temperature of 670°C (Fig. 3a). With regard to the decrease in the creep rate at 670 and 700°C (Figs. 4a, 4b), the positions of the steels are similar. The maximum high-temperature strength is characteristic of the EP-450-DUO steel. In particular, the time to fracture of the oxide-dispersion strengthened EP-450-DUO steel at 700°C and 100 MPa is almost three orders of magnitude larger than for the highest-temperature oxide-free ChS-139 steel (see Fig. 3b and Table 5). The curves of the long-term strength of the investigated steels at 670 and 700°C are presented in Figs. 5a, 5b. The highest values of the long-term strength at 700°C are characteristic of the EP-450-DUO steel and among the carbon-containing steels, these are the ChS-139 and EP-450 steels.

Structural Changes in the Reactor Steels and the Reasons for Different Creep Resistance

Structural studies showed that, during creep tests at 650, 670, and 700°C, in all reactor steels, the degradation of the lath martensitic structure occurs, which is accompanied by the spherodization and coarsening of the chromium-containing carbide $M_{23}C_6$ phase. As can be seen in Fig. 6, after tests at enhanced temperatures and stresses (700°C and 100–140 MPa), which lead to the fairly rapid fracture of the samples (in dozens of hours), a different change in the structure of the different steels is observed. In the ChS-139 and EK-181 steels under a stress of 140 MPa, processes of the coarsening of carbides and the polygonization of martensite occur with a decrease in the density of dislocations, as well as the formation of the dislocation-free subgrains inside the martensitic laths (Figs. 6a, 6b).

In ChS-139 steel, more regions with a high density of dislocations are retained. The time to fracture of this steel is 53.4 h, which is almost three times greater

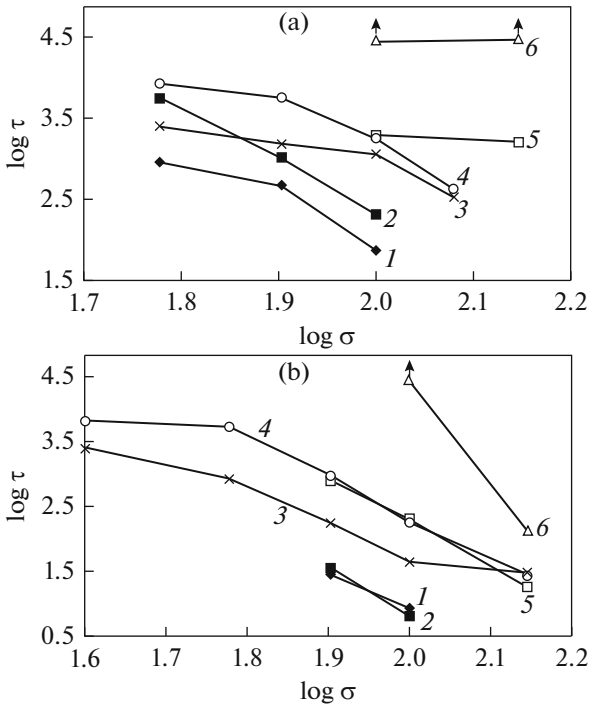

Fig. 3. Relationship between time to fracture and stress in tests of transverse samples of the investigated steels depending of temperature: (*1*) EP-823; (*2*) EP-900; (*3*) EK-181; (*4*) ChS-139; (*5*) EP-450; and (*6*) EP-450-DUO; test temperatures: (a) 650°C for steels *5* and *6*; (a) 670°C for steels *1–4*; and (b) 700°C for steels *1–6*.

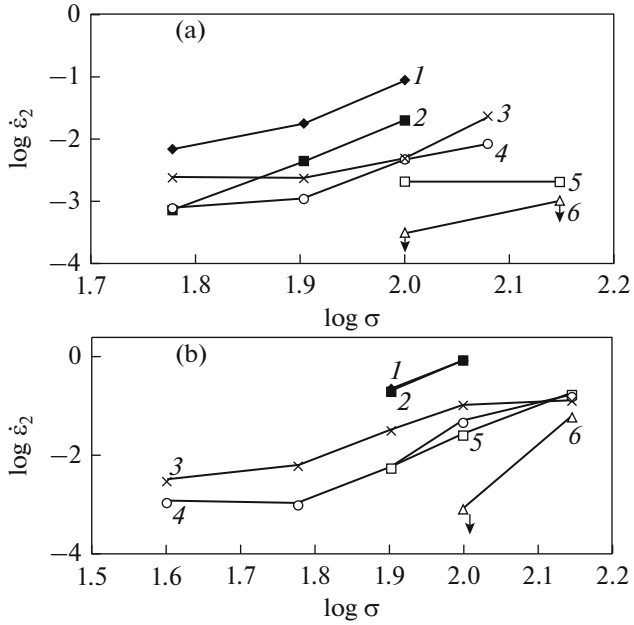

Fig. 4. Dependence of creep rate of transverse samples of (*1*) EP-823, (*2*) EP-900, (*3*) EK-181, (*4*) ChS-139, (*5*) EP-450, and (*6*) EP-450-DUO steels on stresses at various test temperatures: (a) 650°C for steels *5* and *6;* and (b) 670°C (*1–4*), and 700°C (*1–6*).

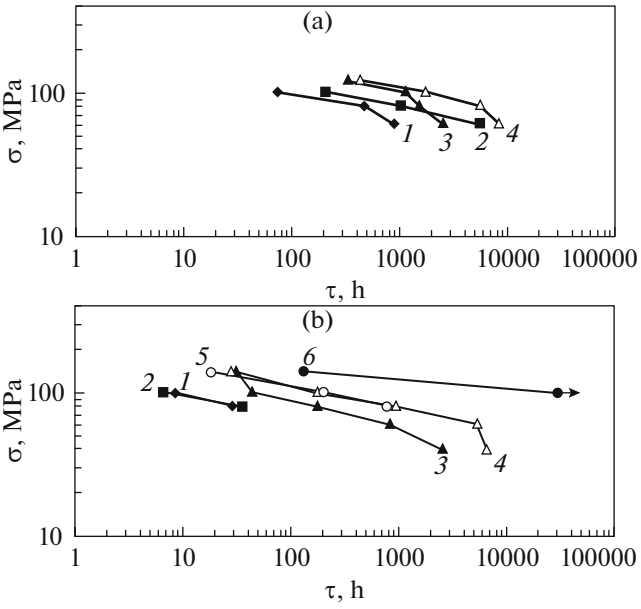

Fig. 5. Long-term strength of the transverse samples of the steels (*1*) EP-823, (*2*) EP-900, (*3*) EK-181, (*4*) ChS-139, (*5*) EP-450, and (*6*) EP-450-DUO at the test temperature of (a) 670 and (b) 700°C.

than that of the EK-181 steel (18.7 h). During a creep test of EK-181 steel at 700°C (σ = 100 MPa, τ_f = 44–67 h), an increase in the average size of chromium carbides from 65 to 112 nm and a decrease in the total number density of particles from 1.2×10^{20} to $(3.4–5.0) \times 10^{19}$ m^{-3} are observed. In the highest-temperature ChS-139 steel at 700°C and 100 MPa, the average size of carbide particles increases to a smaller degree from 60 to 90 nm. The increase in the stress to 140 MPa leads to the growth in the particles to 110 nm. Individual regions of the polygonized structure are retained in the EP-450 steel as well at a lower stress of 120 MPa (Fig. 6c). The completely recrystallized structure (with the elimination of regions of the lath martensitic structure) is observed in the lest high-temperature resistant EP-823 and EP-900 steels after 6.6–8.6 h at a stress of 100 MPa (Fig. 6d, 6e).

During long-term tests at 650–670°C (for thousands of hours), in the most high-temperature resistant ChS-139 and EK-181 steels, the growth of carbide particles and the retaining of the polygonized structure within the martensitic laths are also observed. In the other steels, there occurs a recrystallization with the growth of the grain and active coarsening of the $M_{23}C_6$ carbides (Figs. 7a–7e).

It should be noted that the size of the dispersed carbides of the (V, Nb)C type is also somewhat increased during creep tests, which can be seen on the example of EK-181 steel (Fig. 8). The factor responsible for the increase in the thermal stability of the structure of the ChS-139 steel upon prolonged high-temperature annealings or creep tests may be the higher carbon

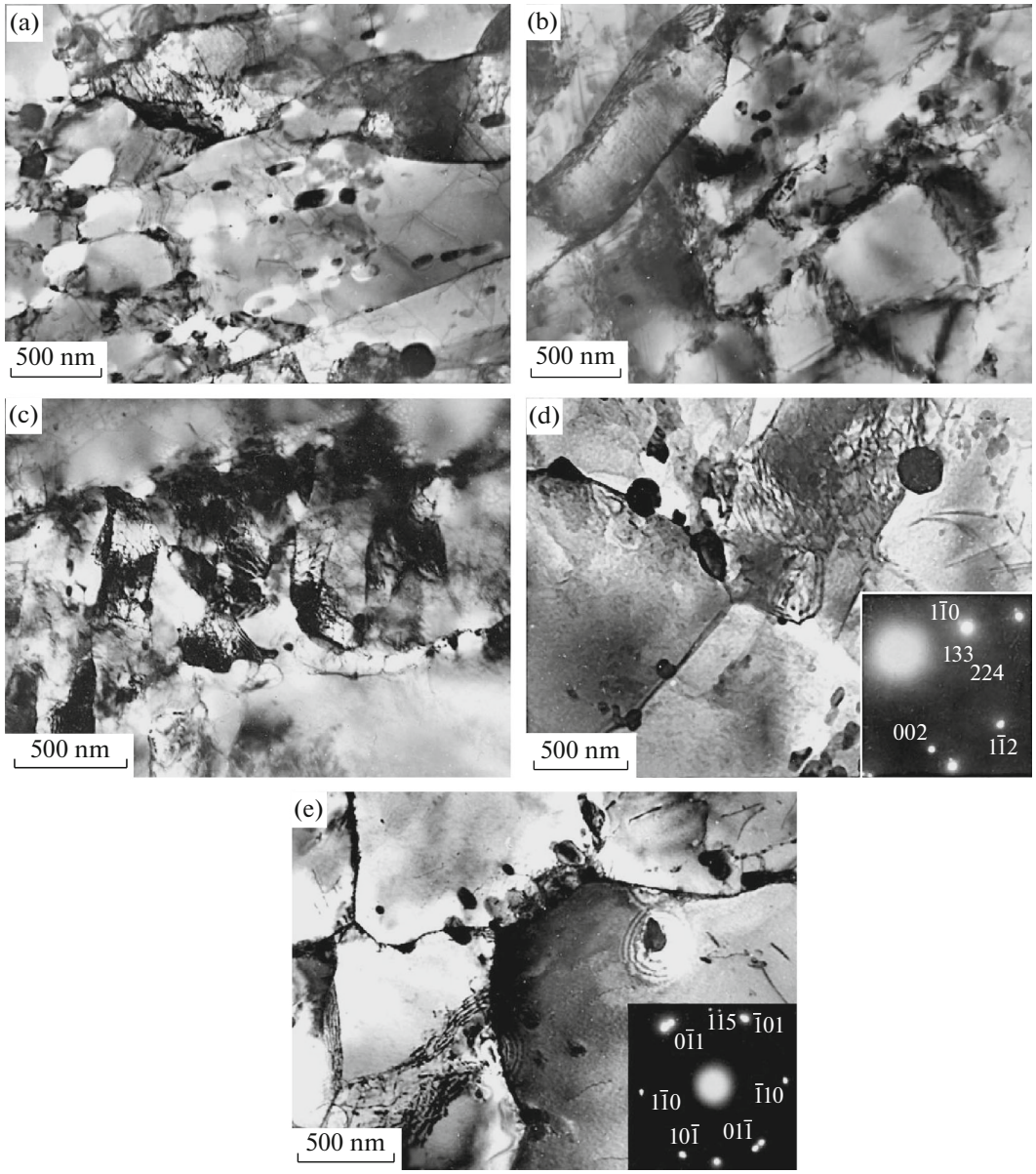

Fig. 6. Structure of (a) ChS-139, (b) EK-181, (c) EP-450, (d) EP-823, and (e) EP-900 steels after short-term creep at 700°C. Creep characteristics (stress and time to fracture) are as follows: (a) 140 MPa, 53.4 h; (b) 140 MPa, 18.7 h; (c) 120 MPa, 125 h; (d) 100 MPa, 8.6 h; and (e) 100 MPa, 6.6 h.

content (0.21 wt % versus 0.13–0.16 wt % in the other steels (Table 1), which provides the formation of a higher amount of carbides of the $Cr_{23}C_6$ type, which inhibit the migration of the boundaries of grains and subgrains. The second reason for the high thermal stability of the ChS-139 steel may be the higher total content of refractory elements Mo, W, Nb, V, and Ta (2.52 wt % versus 1.48 wt % in the EK-181 steel and 1.7–2.1 wt % in the EP-823 and EP-900 steels). In the EP-450 steel, the high-temperature strength is enhanced due to the large number of Mo, Nb, and V (2.4 wt %). The refractory elements hinder the development of the high-temperature diffusion processes in the matrix of ChS-139 steel and increase the thermal stability of the chromium carbides due to their alloying with these elements. Therefore, the chromium carbides of $M_{23}C$ type alloyed with Nb, V, Mo, and W, which are located at the boundaries of laths of the bcc matrix, coalesce to a lesser degree and inhibit the migration of the interlath boundaries upon prolonged high-temperature annealing more strongly.

Structure of the Oxide-Dispersion Strengthened EP-450-DUO Steel

Figure 9 shows the initial structure of the most heat-resistant EP-450-ODS steel and the histogram of the size distribution of the dispersed oxide particles. In

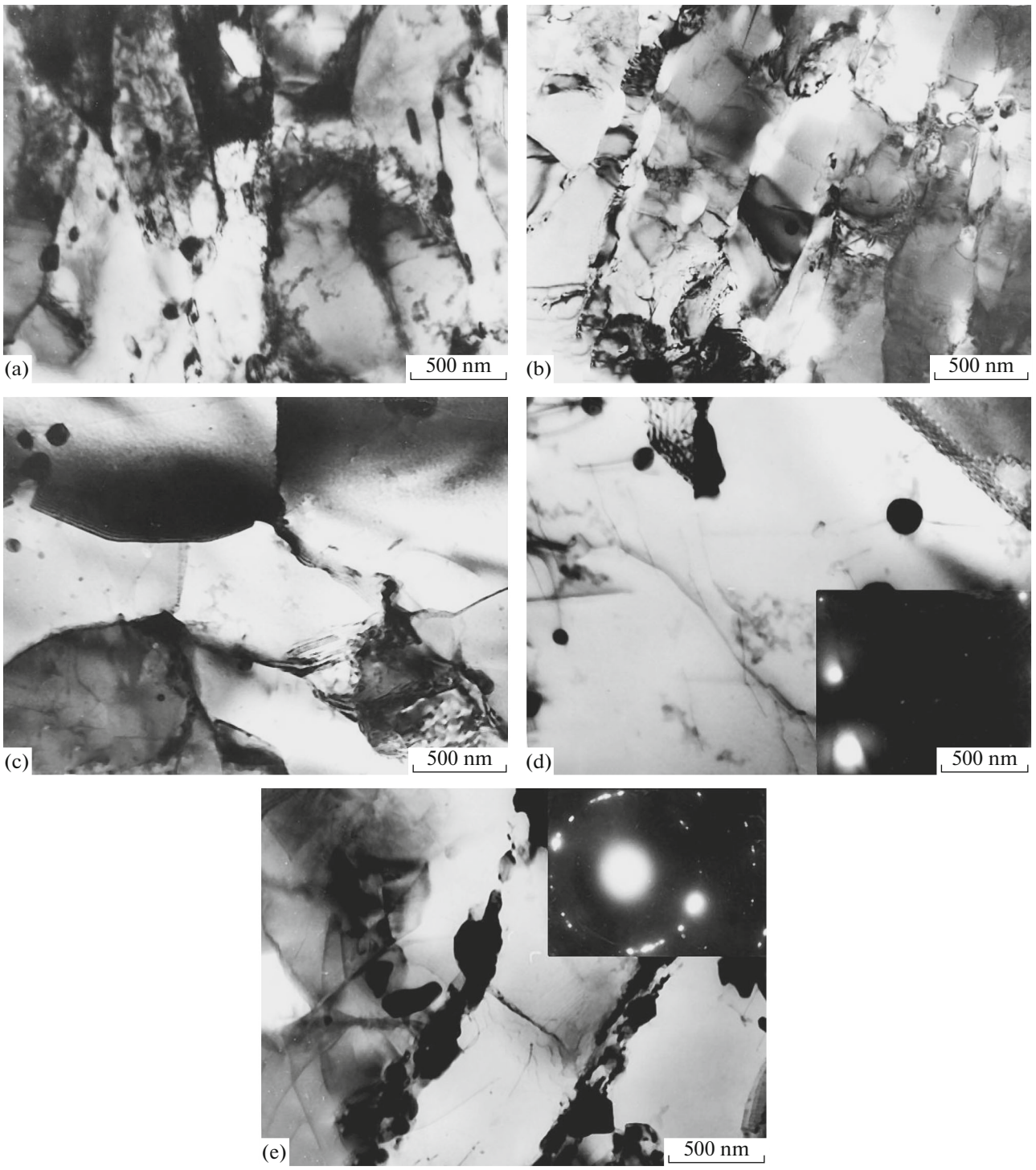

Fig. 7. Structure of the (a) ChS-139, (b) EK-181, (c) EP-450, (d) EP-823, and (e) EP-900 steels after long-term creep at (a–c) 650 and (d, e) 670°C. Creep characteristics (stress and time to fracture): (a) 100 MPa, 7085 h; (b) 100 MPa, 4061 h; (c) 100 MPa, 1938 h; (d) 80 MPa, 470 h; and (e) 80 MPa, 1027 h.

the structure, coarse initial Y_2O_3 oxides with a sizes of 200 nm and less are observed that were fragmented upon processing in the mill but did not dissolve in the bcc matrix of the EP-450 steel. Upon processing in the ball mill, the partial dissolution of the initial oxides that lead to alloying with oxygen and yttrium of the matrix of the steel also occurred.

The subsequent high-temperature sintering of the mechanically alloyed powder leads to the precipitation of the strengthening second-phase Y–Ti oxides [16]

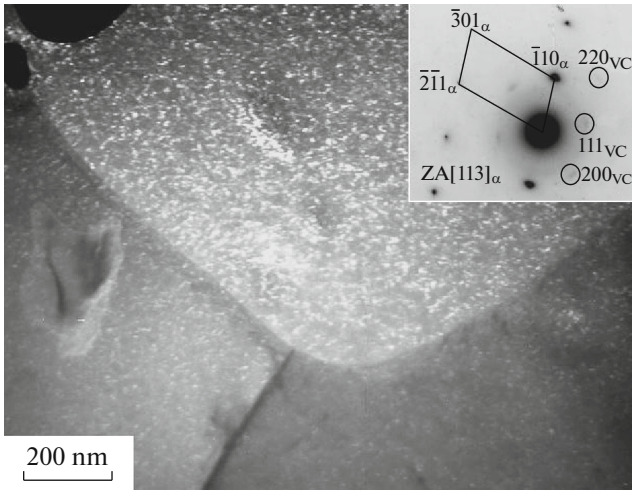

Fig. 8. Dark-field image of the dispersed carbides taken in reflection $(200)_{VC}$ in EK-181 steel after creep tests at 700°C and 80 MPa (time to fracture of 24.6 h).

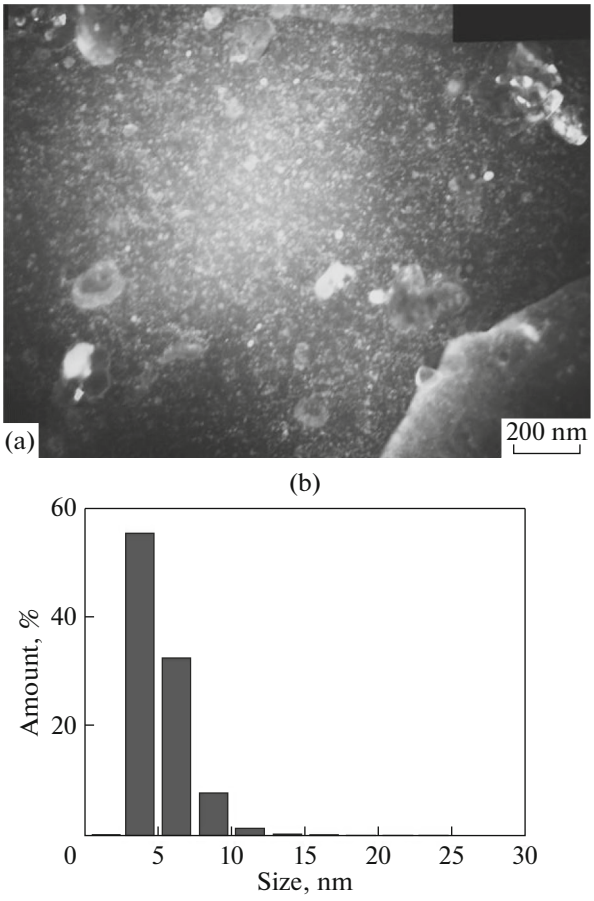

Fig. 9. Structure of EP-450-DUO steel in the initial state (quenching from 1150°C after holding for 1 h and tempering at 740°C for 2 h): (a) bright-field image in the reflection of the yttrium–titanium oxide; and (b) size distribution of second-phase oxides with sizes of less than 20 nm.

with prevailing sizes of less than 20 nm (Fig. 9). As can be seen in the histogram (Fig. 9b), the average size of the fine second-phase oxide particles in the EP-450-ODS is 5 nm and the concentration is 6.7×10^{22} m^{-3}. At 700°C and 100 MPa, the transverse samples of the EP-450-DUO steel were not destroyed until 28000 h, which is greater by two orders of magnitude than the time to fracture of all oxide-free steels with a bcc structure (Fig. 3b). During a 133-h creep test at 700°C and $\sigma = 140$ MPa, the average size of the second-phase oxides is increased to 6 nm and the number density is decreased to 3.6×10^{22} m^{-3} (Fig. 10d). The average size of all particles including coarse ones is 30 nm (Fig. 10c). Despite that the amount of the undissolved coarse particles in the steel is small, these particles occupy a relatively large fraction of the bulk. If we implement a more complete dissolution of the initial oxides upon processing in the ball mill and a correspondingly greater alloying with oxygen of the steel matrix, the amount of the second-phase nanooxides should increase during high-temperature annealing. All of this indicates to the available reserve of the increase in the high-temperature strength of the investigated ODS steel. It should be noted that an increase in the test time of the EP-450-DUO ODS steel almost to 15000 h for longitudinal microsamples at the same temperature of 700°C and stress $\sigma = 140$ MPa causes growth in the secondary oxides to 8 nm and a decrease in their number density to 8.3×10^{21} m^{-3}.

CONCLUSIONS

Long-term high-temperature tests under the loading (of the transverse microsamples cut from the shells of FEs) of the Russian reactor steels with an bcc structure were performed after quenching and high-temperature tempering at 720°C, which leads to the precipitation of carbides of the $Cr_{23}C_6$ and VC types in the ferritic–martensitic structure. The characteristics of the long-term strength, plasticity, and creep rate at 650, 670, and 700°C and stresses of 60, 80, 100, and 140 MPa were determined. It has been found that, from the viewpoint of a decrease in the creep rate, the reactor steels are positioned in the following order: EP-823 and EP-900, EK-181, EP-450 and ChS-139, and EP-450-DUO.

It has been shown that, during long-term holdings under a load in the reactor steels with a bcc structure, the degradation of the lath martensitic structure occurs with a decrease in the number density of dislocations and with the formation of dislocation-free subgrains, as well as the coarsening of the chromium-containing carbide $M_{23}C_6$ phase. The reason for the increase in the thermal stability of the ChS-139 steel upon creep tests is a higher carbon content (0.21 wt %) compared to the other steels, which provides a larger amount of the $Cr_{23}C_6$ carbides, which hinders the migration of the boundaries of grains and subgrains.

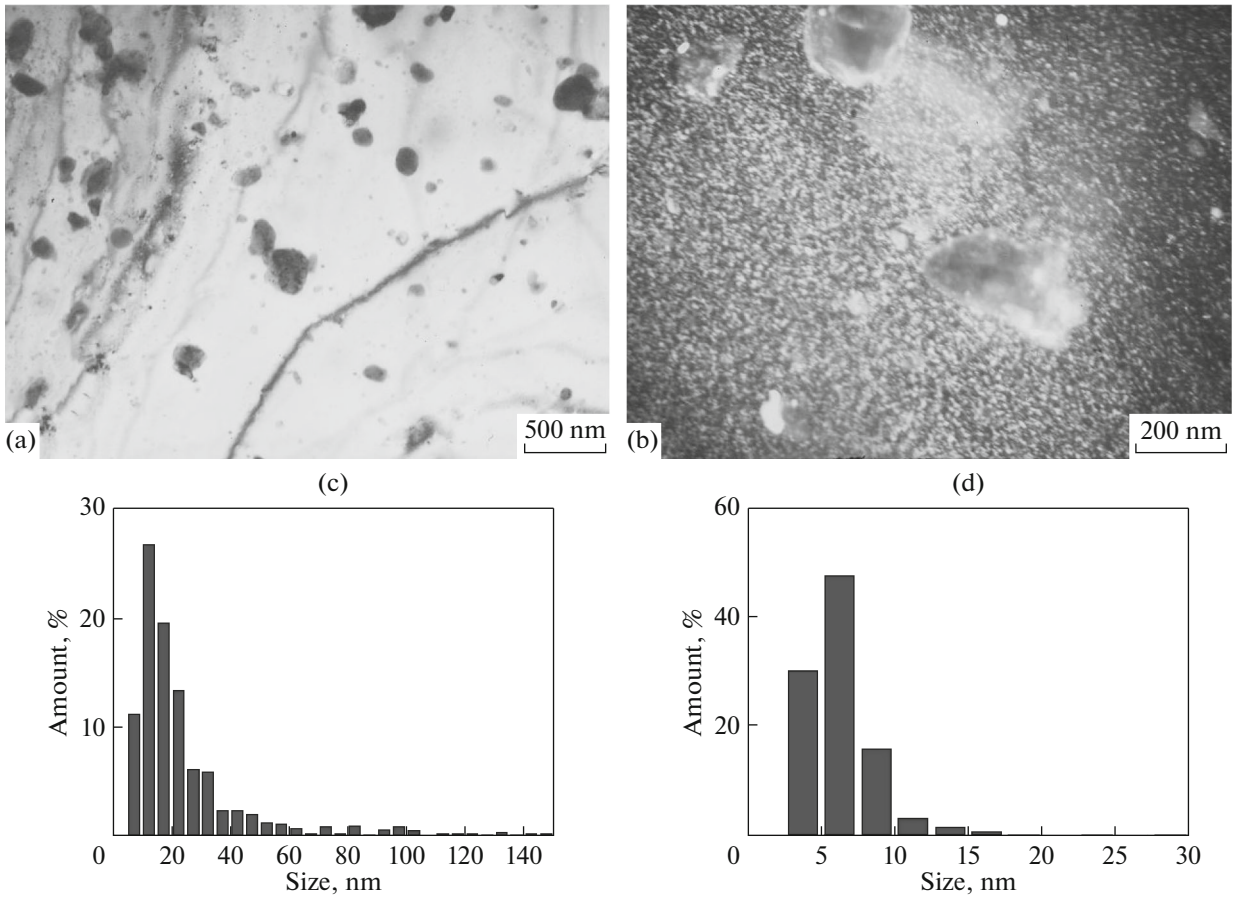

Fig. 10. Structure of samples of the EP-450-DUO steel after creep test at the temperature of 700°C and $\sigma = 140$ MPa (time to fracture, 133 h), and corresponding histograms of the particle-size distribution: (a) bright-field image; (b) dark-field image in the reflection of the yttrium–titanium oxide; (c) size distribution of the oxide particles; and (d) size distribution of the second-phase nanooxides.

The second reason for the high thermal stability of the ChS-139 and EP-450 steels is the maximum total content of refractory elements Mo, W, Nb, V, and Ta (2.40–2.52 wt %), which inhibit the development of the diffusion processes of softening.

Among the investigated steels, the highest long-term strength and creep resistance are characteristic of the oxide-dispersion strengthened EP-450-DUO steel, which contains the most thermally stable yttrium–titanium oxides in the ferritic matrix that have an average size of 5 nm, which increase somewhat in size during long-term tests. At 700°C and 100 MPa, the samples of the EP-450-DUO steel are not destroyed until 28000 h, which is greater by two orders of magnitude than the time to fracture of all oxide-free steels with a bcc structure.

ACKNOWLEDGMENTS

The work was supported in part by the project of the Ural Branch of the Russian Academy of Sciences (theme "Struktura," no. 15-9-2-16). We thank N.M. Zagainova for her assistance in the work.

REFERENCES

1. V. V. Chuev, V. N. Lanskikh, A. N. Ogorodov, A. G. Sheikman, and A. G. Sergeev, "Efficiency of fuel assemblies of fast reactors," in *Studies of Structural Materials of Elements of the Active Zone of Fast Sodium Reactors* (Ural. Otd. Ross. Akad. Nauk, Ekaterinburg, 1994), pp. 85–140.
2. I. A. Portnykh, V. V. Sagaradze, A. V. Kozlov, and L. A. Skryabin, "Relationship of the characteristics of radiation-induced porosity in steel Kh16N15M2GTR (ChS–68) with the temperature and dose of neutron irradiation," Phys. Met. Metallogr. **94**, 95–101 (2002).
3. A. V. Tselishchev, V. S. Ageev, Y. P. Budanov, A. G. Ioltukhovskii, N. M. Mitrofanova, M. V. Leontieva-Smirnova, I. A. Shkabura, L. M. Zabud'Ko, A. V. Kozlov, V. V. Mal'tsev, and A. V. Povstyanko, "Development of structural steel for fuel elements of sodium-cooled fast reactors," Atomic Energy **108**, 274–280 (2010).

4. V. V. Sagaradze, B. N. Goshchitskii, V. L. Arbuzov, and Yu. N. Zuev, "Precipitation-hardening austenitic steel for fast neutron reactors," Metal Sci. Heat Treat. **45**, 293–299 (2003).
5. V. L. Arbuzov, B. N. Gothchitskii, S. E. Danilov, A. E. Kar'kin, V. D. Parkhomenko, V. V. Sagaradze, A. G. Zaluzhnyi, and Y. N. Zuev, "Accumulation and annealing of radiation defects and the hydrogen effect thereon in an austenitic steel 16Cr15Ni3Mo1Ti upon low-temperature neutron and electron irradiation," Phys. Met. Metallogr. **117**, 89–98 (2016).
6. P. J. Maziasz, "Overview of microstructural evolution in neutron-irradiated austenitic stainless steels," J. Nucl. Mater. **205**, 118–145 (1995).
7. H. R. Brager, "The effect of cold working and preirradiation heat treatment on void formation in neutron-irradiation type 316 stainless steel," J. Nucl. Mater. **57**, 103–113 (1975).
8. G. R. Odette, "On mechanisms controlling swelling in ferrite and martensite alloys," J. Nucl. Mater. **155–157**, 921–927 (1988).
9. E. Dequidt, J. Arroyo, and M. Schirra, "The mechanical behavior of newly designed low-activation high chromium martensitic steels," J. Nucl. Mater. **179–181**, 659–662 (1991).
10. V. L. Arbuzov, V. I. Voronin, B. N. Goschitskiy, S. E. Danilov, V. A. Kazantsev, N. V. Kataeva, V. V. Sagaradze, V. M. Chernov, M. V. Leontieva-Smirnova, and E. M. Mozhanov, "Features of structural and phase states and physical properties of the ferritic and martensitic steel EK-181 after different thermal treatment," Vopr. At. Nauki Tekhn. Ser.: Mater. Nov. Mater. No. **1**, 8–21 (2015).
11. V. M. Chernov, M. V. Leont'eva-Smirnova, M. M. Potapenko, N. A. Polekhina, I. Yu. Litovchenko, A. N. Tyumentsev, E. G. Astafurova, and L. P. Khromova, "Structure phase transformations and physical properties of ferritic-martensitic 12% chromium steels EK-181 and ChS-139," Tech. Phys. **61**, 97–102 (2016).
12. A. N. Tyumentsev, V. M. Chernov, M. V. Leont'eva-Smirnova, E. G. Astafurova, N. A. Shevyako, and I. Yu. Litovchenko, "Microstructure of EK-181 ferritic-martensitic steel after heat treatment under various conditions," Tech. Phys. **57**, 48–54 (2012).
13. A. N. Orlov, A. M. Parshin, and Yu. V. Trushin, "Physical aspects of decrease of irradiation swelling of structural alloys," Zh. Tekhn. Fiz. **53**, 2367–2372 (1983).
14. V. V. Sagaradze, V. M. Nalesnik, S. S. Lapin, and V. M. Aliabev, "Precipitation hardening and radiation damageability of austenitic stainless steels," J. Nucl. Mater. **202**, 137–144 (1983).
15. V. V. Sagaradze and S. S. Lapin, "Inconventional approaches to the suppression of irradiation-induced swelling of stainless steels," Phys. Met. Metallogr. **83**, 417–427 (1997).
16. V. S. Ageev, A. A. Nikitina, B. V. Safronov, V. V. Tsvelev, A. P. Chukanov, N. F. Vil'danova, K. A. Kozlov, T. N. Kochetkova, and V. V. Sagaradze, "Structure and thermal creep of the oxide-dispersion-strengthened EP-450 reactor steel, " Phys. Met. Metallogr. **106**, 318–325 (2008).
17. V. V. Sagaradze, V. I. Shalaev, V. L. Arbuzov, B. N. Goshchitskii, T. Yun, Q. Wan, J. Sun, "Radiation resistance and thermal creep of ODS ferritic steels," J. Nucl. Mater. **295**, 265–272 (2001).
18. S. Ukai, M. Harada, and H. Okada, "Alloying design of oxide dispersion strengthened ferritic steel for long life FBRs core materials," J. Nucl. Mater. **204**, 65–73 (1993).
19. I. Monnet, P. Dubuisson, Y. Serruys, M. O. Ruault, O. Kaitasov, and B. Jouffrey, "Microstructural investigation of the stability under irradiation of oxide dispersion strengthened ferritic steels," J. Nucl. Mater. **335**, 311–321 (2004).
20. C. Crayton, E. Rath, I. Chu, and S. Launois, "Microstructural evolution of Y_2O_3 and $MgAl_2O_4$ ODS EUROFER steels during their elaboration by mechanical milling and hot isostatic pressing," J. Nucl. Mater. **335**, 83–102 (2004).
21. I. Hilger, M. Tegel, M. J. Gorley, P. S. Grant, T. Weibgarber, and B. Kieback, "The structural changes of Y_2O_3 in ferritic ODS alloys during milling," J. Nucl. Mater. **447**, 242–247 (2014).
22. M. Klimiankou, R. Lindau, and A. Möslang, "HRTEM study of yttrium oxide particles in ODS steels for fusion reactor application," J. Crystal Growth **249**, 381–387 (2003).

Translated by O. Golosova